8

OPTICAL EXTINCTION OF METAL NANOPARTICLES SYNTHESIZED IN POLYMER BY ION IMPLANTATION

A. L. Stepanov

Kazan Physical–Technical Institute of the Russian Academy of Sciences, Kazan, Russian Federation; and Institute for Experimental Physics and Erwin Schrödinger Institute for Nanoscale Research, Karl-Franzens-University Graz, Graz, Austria

1. INTRODUCTION

The problem of designing new polymer-based composite materials containing metal nanoparticles (MNPs) is of current interest, particularly in the fabrication of magnetooptic data storages, picosecond optical switches, directional connectors, and so on. The nonlinear optical properties of these composites stem from the dependence of their refractive index on incident light intensity. This effect is associated with MNPs, which exhibit a high nonlinear susceptibility of the third order when exposed to ultrashort (picosecond or femtosecond) laser pulses [1].

Light-induced electron excitation in MNPs (so-called surface plasmon resonance, SPR) [2], which shows up most vividly in the range of linear absorption) gives rise to nonlinear optical effects in the same spectral range. Therefore, in practice, the SPR effect may be enhanced by raising the

Metal-Polymer Nanocomposites, Edited by Luigi Nicolais and Gianfranco Carotenuto
ISBN 0-471-47131-3

nanoparticle concentration in the composite—that is, by increasing the volume fraction of the metal phase (filling factor) in the insulator. Systems with a higher filling factor offer a higher nonlinear cubic susceptibility, when all other things being the same [1].

Metal particles may be embedded in a polymer matrix in a variety of ways. These are chemical synthesis in an organic solvent [2], vacuum deposition on viscous-flow polymers [3], plasma polymerization combined with metal evaporation [4], and so on. However, they all suffer from disadvantages, such as a low filling factor or a great spread in size and shape of particles synthesized, which offsets the good optical properties of composites.

One more promising method is ion implantation [5], which provides controllable synthesis of MNPs at various depths under the surface and unlimitedly high-impurity doses. Despite the intensive study of metal nanoparticle synthesis by ion implantation in dielectrics, such as nonorganic glasses and crystals, which was started in 1973 by Davenas et al. with Na and K ions [6] and in 1975 by Arnold with Au ions [7], the formation of nanoparticles in organic matrices was realized only at the beginning of the 1980 by Koon et al. in their experiments on implantation of Fe ions into polymers [8]. By implantation, one can produce almost any metal–insulator (specifically, metal–polymer) composites, as follows from Table 8.1, which gives a comprehensive list of references [9–40], MNP shapes, and implantation conditions for various organic matrices. Note that noble metals exhibit the most pronounced SPR effect and, hence, the highest nonlinearity of the MNP optical properties in insulators [2]. This chapter focuses on polymer-based optical materials containing metallic nanoparticles (Ag, Au, etc.) characterized by SPR. Only recently were such materials fabricated by Ag implantation into epoxy resins [38] and polymethylmethacrylate (PMMA) [18, 33–35]. However (see, e.g., references 33 and 34), an unusually weak plasmon resonance absorption was detected in the case of the Ag–PMMA composite despite the high concentration of the synthesised Ag nanoparticles. The aim of this work is therefore to study the SPR-related linear optical properties of MNPs introduced into a polymer matrix by implantation. We compare experimental optical spectra for silver nanoparticles implantation-synthesized in PMMA with model spectra calculated based on the Mie classical electrodynamic theory [2, 41].

2. EXPERIMENTAL

As substrates, 1.2-mm-thick PMMA plates, which are optically transparent in a wide spectral range (400–1000 nm), were used [42]. Substrates were implanted by 30-keV Ag^+ ions with doses in the range from 3.1×10^{15} to $7.5 \times$

TABLE 8.1. Conditions for MNP Synthesis by Ion Implantation into Polyvinylidene Fluoride (PVF_2), Polyimide (PI), Polymethylmethacrylate (PMMA), Polymethylmethacrylate with Phosphorus-Containing Fragments (PMMA + PF), Polyethylene (PE), Poly(ethyleneterephthalate) (PET), Silicone Polymer (Phenylmethyl-silane Resin with Tin Diethyldicaprilate), Epoxy Polycarbonate (PC), and Polyetherimide (PEI)[a]

Metal of Particles	Matrix	Ion Beam Energy (keV)	Ion Dose (ion/cm^2)	Ion Current Density (μA/cm^2)	Substrate Temperature (K)	Shape of Particles	Study Methods	Authors
Ti	PET	40	2.0×10^{17}	4.5			TEM XRD	Wu et al. 2001 [9]
Cr	PET	40	1.0×10^{17}	4.5			TEM XRD	Wu et al. 2000 [10]
Fe	PVF_2	25	$0.1–1.0 \times 10^{17}$	—	300		FMR	Koon et al. 1984 [8]
Fe	PM	100–150	$0.1–1.0 \times 10^{17}$	0.1–5	300	Spherical	TEM	Ogawa 1988 [11]
Fe	PM	40	$0.25–1.2 \times 10^{17}$	4, 8, 12	300	Spherical and their aggregates	TEM FMR	Khaibullin R.I. et al. 2002 [12] Popok et al. 2002 [13]
Fe	PMMA	100–150	$0.1–1.0 \times 10^{17}$	0.1–5	300	Spherical	TEM	Ogawa 1988 [11]
Fe	PMMA	40	$0.1–6.0 \times 10^{17}$	1–10	300	Spherical and their aggregates	TEM FMR	Petukhov et al. 1993 [14] 1995 [15] 1996 [16] 2001 [17] Bazarov et al. 1995 [18]
Fe	PMMA–PF	40	$1.0–3.0 \times 10^{16}$	1–6	300	Spherical and their aggregates	TEM FMR	Petukhov et al. 2001 [17]

TABLE 8.1. Continued

Metal of Particles	Matrix	Ion Beam Energy (keV)	Ion Dose (ion/cm^2)	Ion Current Density (μA/cm^2)	Substrate Temperature (K)	Shape of Particles	Study Methods	Authors
Fe	PE	25	$0.1–1.0 \times 10^{17}$	—	300		FMR	Koon et al. 1984 [8]
Fe	PET	100–150	$0.1–1.0 \times 10^{17}$	0.1–5	300	Spherical	TEM	Ogawa 1988 [11]
Fe	PET	40	$1.0–3.0 \times 10^{16}$	1–6	300		TEM FMR	Petukhov et al. 2001 [17]
Fe	Silicone polymer	40	$0.3–1.8 \times 10^{17}$	4	300	Spherical and their aggregates	TEM	Khaibullin R.I. et al. 1998 [19] 1999 [20] 2000 [21] Rameev et al. 2000 [22]
Co	PM	100–150	$0.1–1.0 \times 10^{17}$	0.1–5	300	Spherical	TEM	Ogawa 1988 [11]
Co	PM	40	$0.25–1.2 \times 10^{17}$	4, 8, 12	300	Spherical and their aggregates	TEM	Popok et al. 2002 [13]
Co	Silicone polymer	40	$0.3–1.8 \times 10^{17}$	4	300	Spherical and their aggregates	TEM FMR	Khaibullin R.I. et al. 2000 [21] Rameev et al. 2000 [22]
Co	Epoxy	40	$0.3–2.5 \times 10^{17}$	2–8	300	Spherical, needle-like, drop-like, cubic-faced, and so on.	TEM	Stepanov et al. 1994 [23] 1995 [24] Abdulin et al. 1996 [25] 1996 [26] 1998 [27] Khaibullin R.I. et al. 1996 [28]

								Khaibullin I.B. et al. 1997 [29]
Cu	PM	150	$0.5–1.0 \times 10^{17}$	1–5	<360	Spherical	TEM	Yushida and Iwaki 1987 [30]
Cu	PM	80 100	5.0×10^{16}	0.1	<630	Spherical	TEM	Kobayashi et al. 2001 [31]
Cu	PMMA	40	$0.1–6.0 \times 10^{17}$	1–6	360	Spherical	TEM	Petukhov et al. 2001 [17]
Cu	PMMA–PF	40	$1.0–3.0 \times 10^{16}$	1–6	360	Spherical	TEM	Petukhov et al. 2001 [17]
Cu	PET	40	$0.5–2.0 \times 10^{17}$	4–5	360	Spherical	TEM AFM XRD	Wu et al. 2000 [10] 2001 [32]
Cu	PET	40	$1.0–3.0 \times 10^{16}$	1–6	360	Spherical	TEM	Petukhov et al. 2001 [17]
Zn	PM	150	5.0×10^{17}	1–5	<360	Spherical	TEM	Yoshida and Iwaki 1987 [30]
Pd	PM	100	$0.1–1.0 \times 10^{17}$	0.1	<630	Spherical	TEM	Kobayashi et al. 2001 [31]
Ag	PM	130	$0.1–5.0 \times 10^{17}$	1–3	<630	Spherical	TEM	Kobayashi et al. 2001 [31]
Ag	PMMA	30	$1.0–7.5 \times 10^{16}$	4	300	Spherical	TEM OS	Stepanov et al. 1994 [33] 2000 [34] 2002 [35] Bazarov et al. 1995 [18]

TABLE 8.1. Continued

Metal of Particles	Matrix	Ion Beam Energy (keV)	Ion Dose (ion/cm^2)	Ion Current Density (μA/cm^2)	Substrate Temperature (k)	Shape of Particles	Study Methods	Authors
Ag	PET	79	$0.5–2.0 \times 10^{17}$	4.5	—	Spherical	TEM	Wu et al. 2000 [10] 2001 [9] 2002 [36]
Ag	Silicone polymer	30	$0.6–1.8 \times 10^{17}$	4	300	Spherical and their aggregates	TEM OS	Khaibullin R.I. et al. 1998 [19] 1999 [20] Stepanov et al. 1998 [37]
Ag	Epoxy	30	$0.22–7.5 \times 10^{17}$	4	300	Spherical	TEM OS	Stepanov et al. 1995 [38] 1997 [39] Khaibullin I.B. et al. 1997 [29]
Pt	PC	106	1.0×10^{17}	—	—	Spherical	TEM	Rao et al. 1994 [40]
Pt	PEI	106	1.0×10^{17}	—	—	Spherical	TEM	Rao et al. 1994 [40]

[a] FMR, ferromagnetic resonance; TEM, transmission electron microscopy; AFM, atomic-force microscopy; OS, optical spectroscopy; and XRD, X-ray diffraction.

10^{16} ion/cm^2 at ion current density of 4 μA/cm^2 in a vacuum of 10^{-6} torr using an ILU-3 ion implanter. In a control experiment, Xe-ion implantation into PMMA at the same conditions was performed. Spectra of optical density were measured from 300 to 900 nm at room temperature in air using a dual-beam spectrophotometer Hitachi 330. All spectra were recorded in a standard differential mode in order to normalize substrate effects. The samples obtained were examined with transmittance electron microscopy (TEM) with a Tesla BM-500 microscope and with Rutherford backscattering (RBS) using a beam of 2-MeV $^4He^+$ ions with van de Graff accelerator.

Optical spectra of spherical MNPs embedded in various dielectric media were simulated in terms of the Mie electromagnetic theory [41], which allows one to estimate the extinction cross section σ_{ext} for a wave incident on a particle. This value is related to the light intensity loss ΔI_{ext} of an incident light beam I_0 that passes through a transparent particle-containing dielectric medium due to absorption σ_{abs} and elastic scattering σ_{sca}, where $\sigma_{ext} = \sigma_{abs} + \sigma_{sca}$. Following the Lambert–Beer law, it is obseve

$$\Delta I_{ext} = I_0\left(1 - e^{-\#\sigma_{ext}h}\right) \tag{1}$$

where h is the thickness of the optical layer and # is the density of nanoparticles in a sample. The extinction cross section is connected to the extinction constant γ as $\gamma = \#\sigma_{ext}$.

Experimental spectral dependencies of optical density (OD) are given by

$$OD = -\lg(I/I_0) = \gamma \cdot \lg(e) \cdot h \tag{2}$$

Hence, for samples with electromagnetically noninteracting nanoparticles, it is possible to put $OD \sim \sigma_{ext}$. Therefore, experimental OD spectra are compared with model spectral dependences that are expressed through σ_{ext} found from the Mie theory.

3. ION SYNTHESIS OF METAL NANOPARTICLES

Ion implantation is an effective tool for introducing single impurities into the surface layer to a depth of several micrometers [5]. The surface modification of the material depends on its properties, as well as on ion implantation parameters (ion type and energy, ion current density, target temperature, etc.). A critical implantation parameter is ion dose F_0, which determines the implant amount. Depending on the modification of an insulating target (polymers, inorganic glasses, ionic crystals, minerals, etc.), ion implantation may be conven-

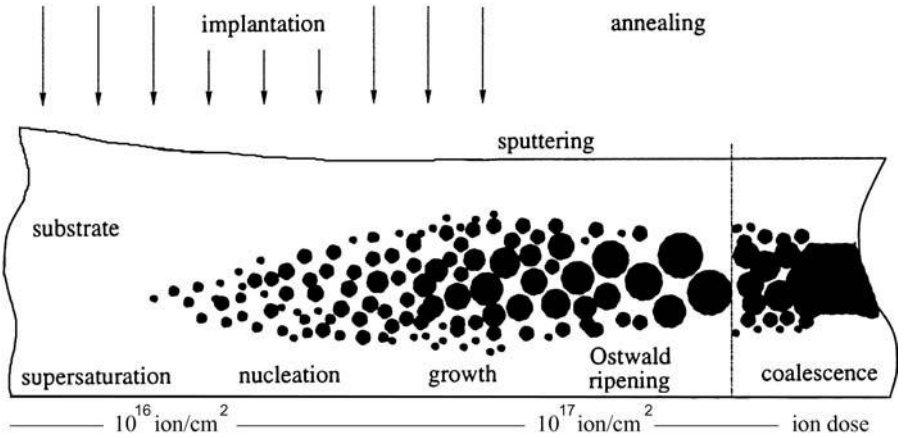

Figure 8.1. Basic physical stages of nanoparticle synthesis by ion implantation versus ion dose.

tionally divided into low-dose and high-dose implantation (Figure 8.1). In the former case ($F_0 \leq 5 \times 10^{14}$ ion/cm^2), the stopped ions are disperse (isolated from one another) in the insulating matrix. The energy of ions implanted is transferred to the matrix through the excitation of electronic shells (ionization) and nuclear collisions. This causes radiation-induced defects, which, in turn, may reversibly or irreversibly modify the material structure [5]. Various types of polymer structure damage have been observed [43]: breaking of covalent bonds in macromolecules, generation of free radicals, cross-linkage, oxidation and carbonization of irradiated layers, formation of new chemical bonds between atoms of the insulator or between ions implanted, and so on. In addition, ion implantation may be accompanied by the intense sputtering of the surface exposed [36, 44] or, sometimes, by the swelling of the polymer [45].

High-dose implantation may also be divided into dose (or time) stages (Figure 8.1). At F_0 between 10^{15} and 10^{16} ion/cm^2, the equilibrium solubility of metallic implants in insulators (in particular, polymers) is usually exceeded, causing the nucleation and growth of MNPs. The dose threshold value depends on the type of the insulator and implant. For 25-keV silver ions implanted into $LiNbO_3$, the threshold dose was found to be $F_0 \approx 5.0 \times 10^{15}$ ion/cm^2 [46]; for 30-keV silver ions implanted into epoxy resin, $F_0 \approx 10^{16}$ ion/cm^2 [38].

At the next stage of high-dose implantation, starting from $F_0 \geq 10^{17}$ ion/cm^2, the existing MNPs coalesce to form MNP aggregates or quasi-continuous films in the surface layer (Figure 8.1). For example, the irradiation of epoxy resin by 49-keV cobalt ions at higher-than-threshold doses favors the formation of thin

labyrinth structures [25, 27]. The MNP distribution established in the insulator after coalescence or Ostwald ripening may be disturbed by postimplantation thermal or laser annealing.

In this work, composites where MNPs are disperse and isolated from one another—that is, synthesized at ion doses of 10^{15}–10^{17} ion/cm^2, were studied. In the present case of implantation by heavy Ag^+ ions at relatively low energy 30 keV, nuclear collisions prevail in ion–insulator interaction. They displace atoms in the polymer matrix and break some of chemical bonds in it. Along with this, target atoms effectively lose electrons and the implanted Ag^+ ions deionize with the formation of neutral silver atoms (Ag^0). In principle, Ag atoms may combine with arising organic radicals and polymer ions or take part in the oxidation reaction. However, because of a great difference in Gibbs free energy between Ag atoms and atoms of PMMA elements, Ag–Ag bonding is energetically more favorable.

The formation of MNPs proceeds in several stages: the accumulation of and subsequent supersaturation by Ag^0 atoms in a local surface region of the polymer, the formation of nuclei consisting of several atoms, and the growth of silver particles from the nuclei. Assuming that the nanoparticles nucleate and grow via the successive attachment of silver atoms (which are neutralized embedded Ag^+ ions), one may conclude that this process is governed simultaneously by the diffusion coefficient and local concentration of silver atoms—that is, depends on the matrix temperature. In this work, ion implantation was performed under identical conditions; specifically, the polymer during irradiation was kept at room temperature.

As follows from electron microscopy data, silver ion implantation under the experimental conditions considered will result in the formation of silver nanoparticles. For example, the cross-sectional micrograph in Figure 8.2 (a dose of 5.0×10^{16} ion/cm^2) shows dark spherical nanoparticles against the bright field (polymer). The irradiation of PMMA by xenon ions did not result in such patterns. Microdiffraction patterns demonstrate that the nanoparticles have the fcc structure of metallic silver. The patterns consist of thin rings (corresponding to polycrystalline nanoparticles) imposed on wide diffuse faint rings from the amorphous polymer matrix. By comparing the experimental diffraction patterns with standard ASTM data, it possible to conclude that implantation does not form any chemical compounds involving silver ions.

From RBS spectra (Figure 8.3), it is seen that the silver implantation layer (i.e., the depth where the nanoparticles are located) is almost independent of the ion dose. The dose dependence is observed only for the silver peak RBS intensities, with the widths and positions of the lines remaining unchanged. It is known that the implantation depth of an ion depends largely on its energy (accelerating voltage) [4], provided that the chemical constitution of the surface

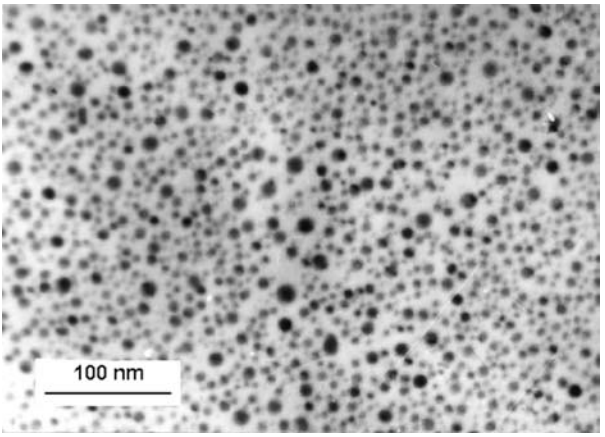

Figure 8.2. Micrograph of silver nanoparticles produced by Ag^+ implantation into PMMA at a dose of 5×10^{16} ion/cm^2.

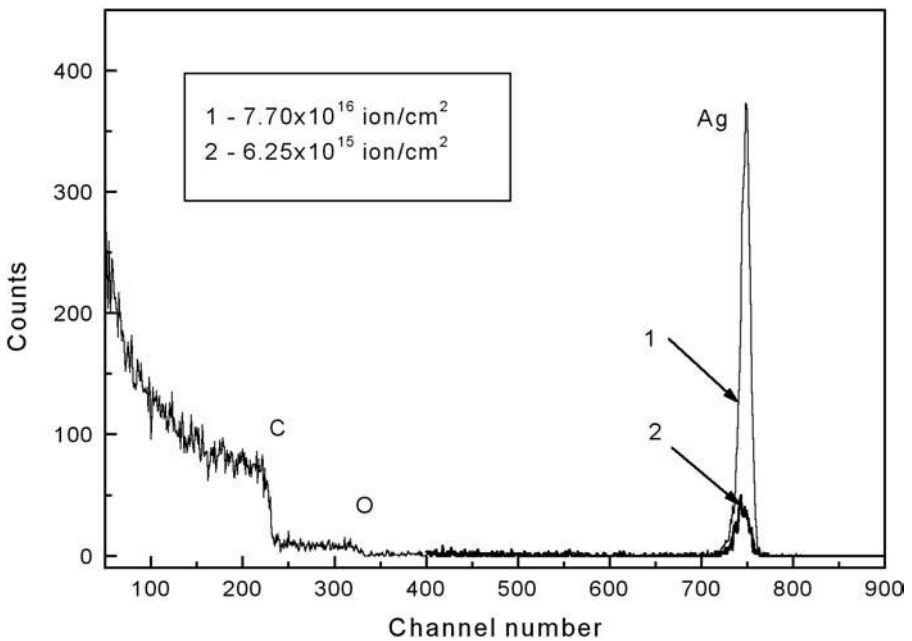

Figure 8.3. RBS spectra from PMMA irradiated by silver ions for doses of (1) 7.7×10^{16} and (2) 6.25×10^{15} ion/cm^2.

irradiated does not change dramatically [44]. The similarity of the RBS spectra shown in Figure 8.3 implies that the arising MNPs do not restrict the penetration depth of silver ions at the higher dose. Thus, in PMMA, the implantation dose, being responsible for the amount of the implant, influences directly the MNP size but does not affect the implant distribution profile at present conditions. As was noted above, the particles nucleate at a dose of ~10^{16} ion/cm^2 (low-dose implantation). For silver in PMMA, this dose provides MNPs with a size of about 2 nm. However, at a dose of 5.0×10^{16} ion/cm^2 (Figure 8.2), the particles grow to 10 nm.

Experimental optical absorption spectra for PMMA irradiated by xenon and silver ions at various doses are shown in Figure 8.4. It is evident that the xenon

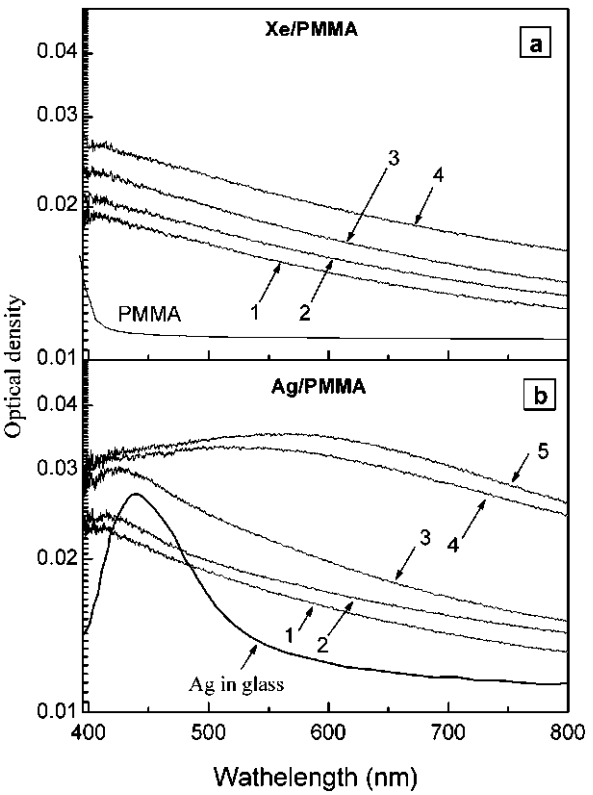

Figure 8.4. Optical density spectra from PMMA irradiated by (**a**) xenon and (**b**) silver ions for doses of (1) 0.3×10^{16}, (2) 0.6×10^{16}, (3) 2.5×10^{16}, (4) 5.0×10^{16}, and (5) 7.5×10^{16} ion/cm^2. The spectrum taken from silica glass irradiated by silver ions (5.0×10^{16} ion/cm^2) [44] is shown for comparison.

irradiation of PMMA does not produce nanoparticles, as also follows from the micrographs (Figure 8.2). In Figure 8.4a, as the xenon ion dose increases, the absorption of the polymer in the visible (especially in the close-to-UV) range also increases monotonically. This indicates the presence of radiation-induced structure defects in the PMMA. The absence of absorption bands in these spectral curves is noteworthy. The implantation of silver not only generates radiation-induced defects but also causes the nucleation and growth of MNPs. Therefore, along with the absorption intensity variation as in Figure 8.4a, an absorption band associated with silver nanoparticles is observed (Figure 8.4b). For the lowest dose, the peak of this band is near 420 nm and shifts to longer waves (up to 600 nm) with dose, with the band broadening significantly. The peak of this band is not high, although it is related to the SPR effect in the silver nanoparticles. The very low intensity of SPR absorption is atypical of silver nanoparticles in PMMA and cannot be explained by the polymer environment of the particles. When silver particles were synthesized in PMMA by the convection technique [47], the SPR intensity was very intense, unlike our experiment. Nor can the weak SPR absorption be explained by any features of the implantation process. For comparison, Figure 8.4 shows the optical density spectrum for inorganic silica glass (SiO_2) irradiated by silver ions under the conditions similar to the ion synthesis conditions used in this work (silica glass has the refractive index $n \approx 1.5$ close to that of PMMA) [44]. It is seen that the absorption of Ag nanoparticles in the glass (Figure 8.4b) is much more intense (even in view of the background absorption due to matrix structure imperfections) than the absorption of the particles in the polymer. Note that the particle size distributions in the glass and PMMA are nearly the same. Below, the optical properties of the Ag–PMMA composite are simulated, and we discuss various effects that may clarify the SPR absorption of Ag nanoparticles synthesized in PMMA by ion implantation.

4. SIMULATION OF OPTICAL EXTINCTION

4.1. Extinction of Silver Particles in Dependence of Surrounding Matrix

The attenuation (extinction) of an optical wave propagating in a medium with MNPs depends on the amount of the SPR effect and the light scattering efficiency. The wavelength of optical radiation, the particle size, and the properties of the environment are governing factors in this process. Within the framework of classical electrodynamics (the Maxwell equations), the problem of interaction between a plane electromagnetic wave and a single spherical particle was exactly solved in terms of optical constants of the interacting objects by Mie [2, 41]. According to the Mie theory, the extinction and scattering cross

sections are expressed as an infinite sum of spherically symmetric partial electric and magnetic waves that generate fields similar to those generated by the particle when it is viewed as an excited multipole. In the general case, the Mie electromagnetic theory imposes no limitations on the wavelength of optical radiation. Therefore, the operation on the optical constants of the particles and matrix results in extinction spectra, so-called Mie resonance bands [2], which agree well with experiment. However, the Mie theory, which relies on the spectral dependence of the optical constants, does not allow one to penetrate deep into the physics of Mie optical peaks exhibited by the particles. Yet, independent investigations [2] into the behavior of silver nanoparticles showed that Mie resonances are due to the SPR effect, so that analytical Mie spectra may be compared with experimental data.

Simulated extinction spectra for Ag nanoparticles embedded in a polymer matrix to compare with experimental data shown in Figure 8.4. In theoretical calculations, we used the complex value of the optical constant ε_{Ag} in the visible range [48] that was obtained by measurements on a set of fine silver particles. Such an approach [48] takes into account limitations imposed on the electron free path in particles of different size and electron scattering at the particle–insulator interface [49] and thus yields a more exact value of ε_{Ag} than does the procedure of correcting optical constants for bulk silver [50]. The complex value of ε_{PMMA} for the polymer matrix was found elsewhere [42]. The extinction was calculated for particles of size between 1 and 10 nm (according to the MNP sizes in Figure 8.2).

At the early stage of simulation, consider the simple case where Ag nanoparticles are incorporated into the PMMA matrix. Associated extinction spectra for different metal particle sizes are shown in Figure 8.5. These spectra feature a wide band, which covers the entire spectral range. In the given range of particle sizes, the position of the SPR absorption maximum (near 440 nm) is almost independent of the particle size. However, the extinction band intensity grows while the band itself somewhat narrows with increasing particle size. Comparing the analytical and experimental spectra, it is seen that, to the greatest extent, Figure 8.5 refers to the situation where PMMA is irradiated by silver ions with doses between 0.33×10^{16} and 2.5×10^{16} ion/cm^2 (Figure 8.4b, curves 1–3). This dose range corresponds to the early stage of MNP nucleation and growth in the *OD* spectral band with a maximum between 420 and 440 nm. Thus, one may conclude that ion implantation in this dose range results in the formation of Ag nanoparticles, as also revealed microscopically. It may be supposed that radiation-induced defects in the PMMA have an insignificant effect on the MNP optical properties in this case. However, at higher implantation doses, the recorded *OD* spectra and the analytical spectra shown in Figure 8.5 diverge; hence, the structure of the metal–polymer composite should be considered.

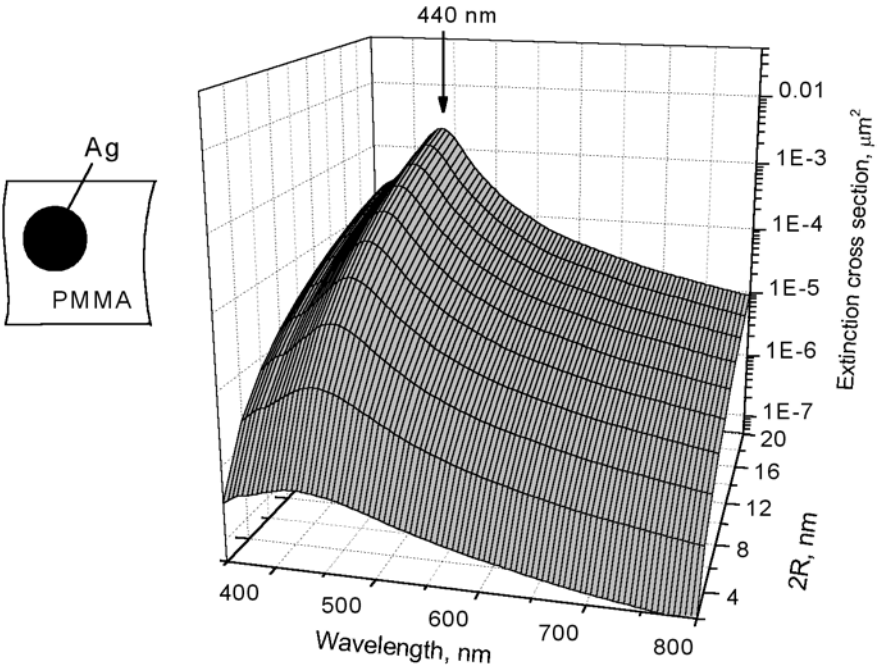

Figure 8.5. Analytical optical extinction spectra for silver nanoparticles embedded in PMMA versus particle size.

To explain the experimental dependences corresponding to high-dose silver implantation into PMMA, we will first elucidate the difference between implantation into polymers and inorganic insulators (silicate glasses, single crystals, minerals, etc.). The most important distinction is that as the absorbed dose grows, so does the number of dangling chemical bonds along the track of an ion. Because of this, gaseous hydrogen, low-molecular hydrocarbons (e.g., acetylene), CO, and CO_2 evolve from the matrix [43]. In particular, ion-irradiated PMMA loses HCOOCH3 methoxy groups [51]. The evolution of several organic fractions leads to the accumulation of carbon in the polymer layer irradiated, and radiation-induced chemical processes may cause chain linking. Eventually, an amorphous hydrogenated carbon layer is produced. Polymer carbonization starts with the formation of polycyclic compounds (in essence, primary carboniferous clusters) and, at higher doses, ends up with the formation of the well-developed carbonized phase via carbon cluster linking.

In view of the specific phase structure of the polymer irradiated, it is of interest to analyze the optical properties (extinction) of Ag nanoparticles embedded in the amorphous carbon matrix (C matrix). For this system, the extinction cross-section spectra versus particle size dependence (Figure 8.6)

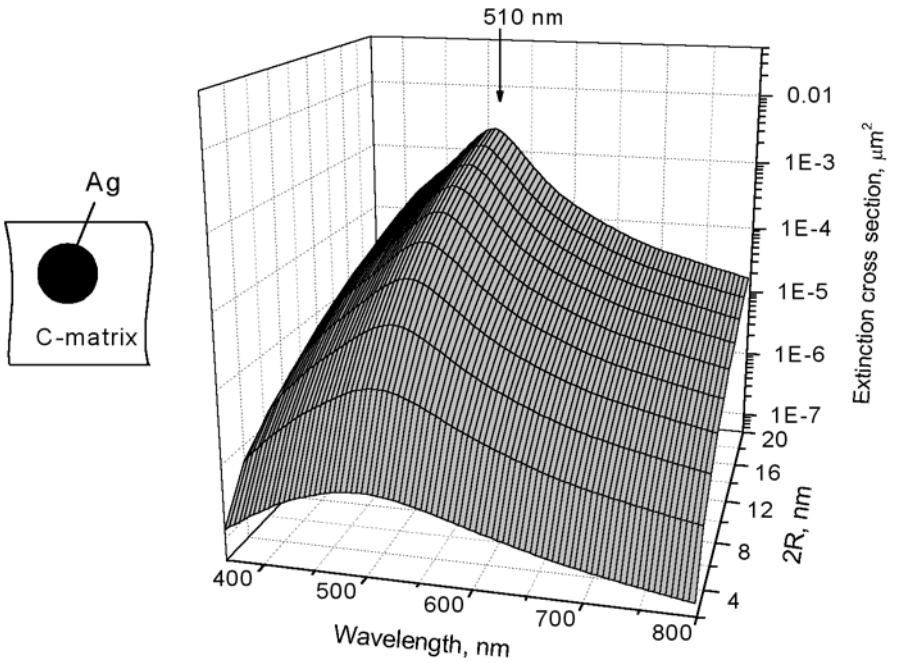

Figure 8.6. Analytical optical extinction spectra for silver nanoparticles embedded in the C matrix versus particle size.

was simulated in the same way as for the MNP–PMMA system—that is, by using complex optical constants ε_C for amorphous carbon, which were taken from reference 52. As before (Figure 8.5), throughout the particle size interval, the extinction spectra exhibit a single broad band, which covers the visible range, with a peak at longer waves (510 nm). The calculated longwave shift of the peak, which is observed upon changing the matrix, may be assigned to a longer wave *OD* band in the experimental spectra for the PMMA, which arises when the Ag ion dose exceeds 2.5×10^{16} ion/cm^2 (Figure 8.4b; curves 3 and 4). It seems that this spectral shift may be associated with the fact that the pure polymeric environment of the Ag nanoparticles turns into the amorphous carbon as the implantation dose rises. The broader extinction bands in the C matrix (Figure 8.6) compared with the PMMA (Figure 8.5) also count in favor of this supposition, since the broadening of the extinction bands is observed in the experiments as well (Figure 8.4b). In a number of experiments, however, the carbonization of the polymer surface layer depended on the type of the polymer and ion, as well as on the process parameters, and completed at doses of $(0.5–5.0) \times 10^{16}$ ion/cm^2 but the entire material was not carbonized. The carbon clusters may reach several tens of nanometers in size [43]. Thus, the assump-

tion that the polymer irradiated is completely carbonized, which was used in the simulation (Figure 8.6), does not become a reality when the process lasts for a long time. Below, the variation of the extinction spectra with amount of carbon in the PMMA layer is analyzed in terms of a model that considers the optical properties of silver MNPs covered by the amorphous carbon sheath.

4.2. Extinction of Silver Particles with Carbon Shell

Extinction spectra for nanoparticles represented as a silver core covered by a carbon sheath in an insulating matrix (PMMA) will be analyzed in terms of the Mie relationships for sheathed cores [53, 54]. Here, an additional interface for which electrodynamic boundary conditions must be set up arises. Plasmon–polariton modes may be excited in both the core and the sheath. These modes, interacting through the inner interface, are responsible for the resulting extinction spectrum.

Optical extinction spectra for a Ag nanoparticle with a fixed size of the core (4 nm) and a varying thickness of the carbon sheath (from 0 to 5 nm) are shown in Figure 8.7. The maximum of the SPR bands of the particles is seen to shift

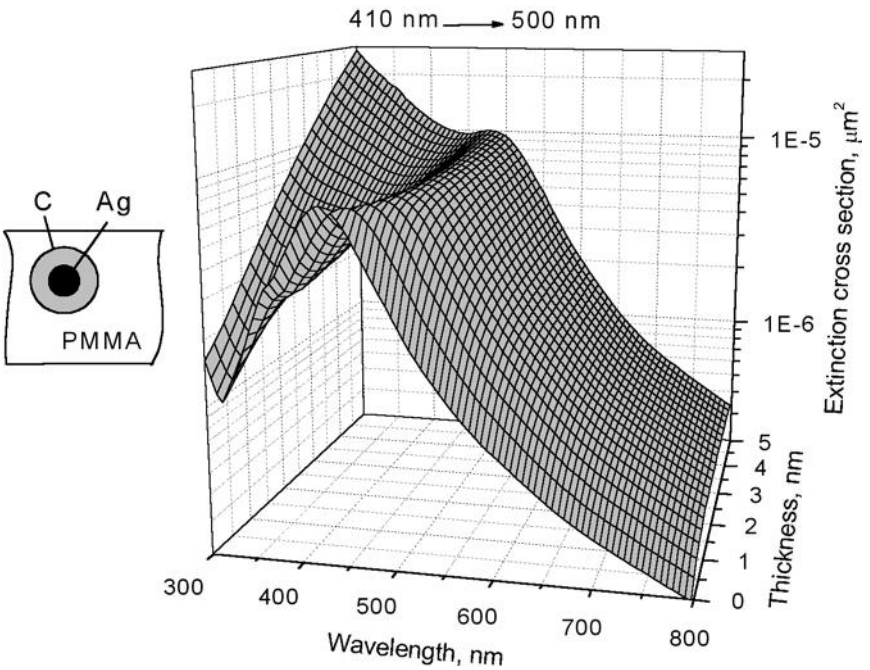

Figure 8.7. Analytical optical extinction spectra for 4-nm silver nanoparticles with the carbon sheath that are placed in the PMMA matrix versus sheath thickness.

from 410 nm (uncovered particle, Figure 8.5) to approximately 510 nm. Simultaneously, the SPR band intensity decreases, while the UV absorption increases, so that the absorption intensity at 300 nm and a sheath thickness of 5 nm exceeds the SPR absorption of the particles. Both effects (namely, the shift of the SPR band to longer waves and the increased absorption in the near ultraviolet) agree qualitatively with the variation of the experimental optical density spectra (Figure 8.4b) when the implantation dose exceeds 2.5×10^{16} ion/cm^2. Thus, our assumption that the increase in the carbonized phase fraction with implantation dose and the variation of the optical density spectra (Figure 8.4b) go in parallel is sustained by the simulation of the optical extinction for complex particles (sheathed cores, Figure 8.7).

In spite of the fact that the model dependences on the carbon sheath thickness and the experimental dose dependences agree qualitatively, discrepancies still exist, particularly in the position of the long-wave maximum in the optical density spectra and in the breadths of the simulated and experimental spectra. Possible reasons for such quantitative discrepancies are discussed below.

4.3. Effects Arising at the Silver Core–Carbon Sheath Interface

Interest in carbon-based composites with MNPs goes back a long way. Examples are the studies of magnetic properties of cobalt particles [55], electric and optical properties of layers with copper [56] or silver [57, 58] nanoparticles, and so on. It was found in optical absorption experiments that copper and silver nanoparticles [56, 58] dispersed in carbon matrices exhibit a weak SPR effect as in our work (Figures 8.4b, 8.6, and 8.7).

When analyzing the optical properties of nanoparticles embedded in a medium, one should take into account effects arising at the particle–matrix interface, such as the static and dynamic redistributions of charges between electronic states in the particles and the environment in view of their chemical constitution [59].

Consider first the charge static redistribution. When an atom is deposited (adsorbed) on the MNP surface, the energy levels of this atom ε_a change their positions compared with those in the free state [59, 60] (Figure 8.8).When the number of the adsorbed matrix atoms becomes significant, their contact generates a wide distribution of density of states. Most frequently, the adsorbed atoms are separated from surface atoms of the metal by a tunnel barrier. The gap between the energy positions ε_a of the adsorbed atoms and the Fermi level ε_F of the particles depends on the type of the adsorbate (Figure 8.8). In addition, the overlap between the energy positions of the matrix atoms and the energy positions of the silver surface atoms depends on the rate with which the electrons tunnel through the barrier. Accordingly, the conduction electron density

in the particles embedded will change compared with that in the particles placed in a vacuum (without adsorbates): It decreases if the electrons tunnel toward the adsorbed atoms, or it increases when the electrons tunnel in the reverse direction. Eventually, equilibrium between the particle and the matrix sets in; that is, a constant electrical charge (Coulomb barrier) forms at the nanoparticle surface.

Such a charge static redistribution due to the deposition of an adsorbate on the particle surface and the respective change in the electron concentration in the MNPs were also observed in the SPR absorption spectra [2, 59]. In metals (silver, sodium, aluminum, etc.), where free conduction electrons dominate, the SPR spectral maximum $h\omega_{max}$ depends on the concentrations of electrons, N, in nanoparticles as

$$h\omega_{max} \approx \left[N/(\varepsilon_0 m_{eff})\right]^{1/2}\left[2\varepsilon_m + 1 + \chi_1^{inter}\right]^{1/2} \tag{3}$$

where ε_m is the permittivity of the matrix, specifying the contribution of the real part of the susceptibility of interband optical transitions in a metal, and m_{eff} is the effective mass of an electron.

It was shown [61] that the incorporation of Ag nanoparticles into the carbon matrix of C_{60} fullerene (or the deposition of carbon on the nanoparticle surface) reduces the concentration of 5*sp* electrons in the particle roughly by 20%, since they are trapped by matrix molecules. According to (equation 3), the decrease in N is bound to shift the MNP extinction spectrum toward longer waves, as also demonstrated by comparing the experimental spectra of the particles in free space (without an adsorbate) with those of the particles in the C_{60} matrix [61]. Samples studied in reference 61 were similar to those obtained by ion implantation in our work (a carbonized layer near silver particles implanted into the polymer). Thus, the shift of the SPR extinction band into the longer wave range with implantation dose in this experiment (Figure 8.4) may be explained by the formation of a carbon sheath around silver nanoparticles. This sheath traps conduction electrons of the particles. The simulation (Figure 8.7) also demonstrates the shift of the SPR maximum. However, the effect of charge dynamic redistribution is disregarded in the Mie theory. Therefore, the long-wave shift of the SPR band due to the charge static redistribution at the particle–matrix interface is an additional reason why the experimental spectra are observed at longer waves than the model ones (Figures 8.6 and 8.7).

Along with the charge static redistribution at the interface, the charge at the same interface may also change dynamically—that is, with a high rate [59]. After the static state of the charge has been established and the Fermi level at the interface has been stabilized, the MNP electrons optically excited above the Fermi level (hot electrons) may tunnel (by fluctuations) to the matrix over or through the static barrier (Figure 8.8). Levels occupied by the electrons in the

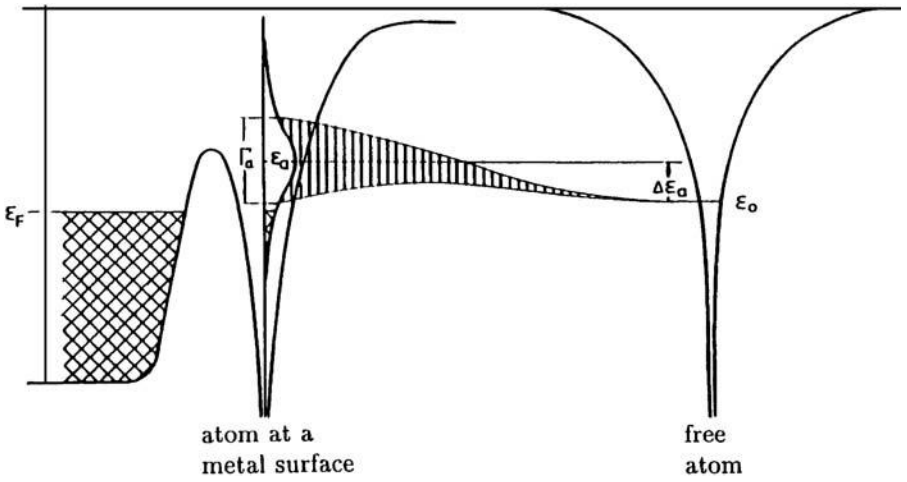

Figure 8.8. Electron energy levels in an atom adsorbed on a metal surface [60]. A free atom (*right*) reaches the surface (*left*). Γ_a is the spread of energy levels ε_a. Electron levels in the conduction band of the metal are occupied up to the Fermi level ε_F.

intermediate (between the particle and the matrix) state depend on the chemical constitution of the materials. Within a residence lifetime, the electrons may tunnel again from the acceptor levels of the matrix to the particle, and this process may occur over and over.

The charge dynamic variation in time at the particle–matrix interface causes the electron concentration in the particle to fluctuate. Fluctuation influences directly the SPR relaxation. The lifetime of excited conduction electrons in the particle defines the SPR spectral width. Here, the contribution from electron scattering by the interface (because of restrictions imposed on the electron free path [4]) adds up with the charge dynamic variation at the interface. Thus, the temporal capture of conduction electrons from the particle broadens the SPR-related extinction spectra. This was demonstrated with a set of silver nanoparticles embedded in the C_{60} matrix [61]. Silver nanoparticles in the carbon matrix exhibit the much broader SPR band than in free space. We may therefore suppose that as the dose rises, the charge dynamic redistribution may broaden the SPR spectra of silver nanoparticles synthesized by ion implantation in PMMA. This is because implantation carbonizes the irradiated layer with increasing absorbed dose and raises the amount of acceptor levels on the MNP surface, which change the relaxation time of electrons excited. Since the classical Mie theory disregards the charge dynamic redistribution, the model spectra (Figure 8.7) must be narrower than the experimental spectra, which is the case.

5. SUMMARY

In this chapter, we studied the formation of silver nanoparticles in PMMA by ion implantation and optical density spectra associated with the SPR effect in the particles. Ion implantation into polymers carbonizes the surface layer irradiated. Based on the Mie classical electrodynamic theory, optical extinction spectra for silver nanoparticles in the polymeric or carbon environment, as well as for sheathed particles (silver core + carbon sheath) placed in PMMA, as a function of the implantation dose are simulated. The analytical and experimental spectra are in qualitative agreement. At low doses, simple monatomic silver particles are produced; at higher doses, sheathed particles appear. The quantitative discrepancy between the experimental spectra and analytical spectra obtained in terms of the Mie theory is explained by the fact that the Mie theory disregards the charge static and dynamic redistributions at the particle–matrix interface. The influence of the charge redistribution on the experimental optical spectra taken from the silver–polymer composite at high doses, which cause the carbonization of the irradiated polymer, is discussed. Table 8.1, which summarizes available data for ion synthesis of MNPs in a polymeric matrix, and the references cited therein may be helpful in practice.

ACKNOWLEDGMENTS

I wish to thank the Alexander Humboldt Foundation for the financial support of the investigations made in Germany; the Austrian Scientific Foundation under the auspices of the Lisa Meitner program; and the State Foundation in Support of Leading Scientific Schools of the Russian Federation (grant no. SS 1904.2003.2). My special thanks go to S. N. Abdullin and V. I. Nuzhdin for the assistance in carrying out an implantation and electron microscopy study, and I also thank D. E. Hole (University of Sussex, United Kingdom) for taking RBS spectra.

REFERENCES

1. C. Flytzanis, F. Hache, M. C. Klein, D. Ricard, and P. Rousignol, *Nonlinear Optics in Composite Materials*, Elsevier Science, Amsterdam (1991).
2. U. Kreibig and M. Vollmer, *Optical Properties of Metal Clusters*, Springer, Berlin (1995).
3. S. N. Abdullin, A. L. Stepanov, Yu. N. Osin, and I. B. Khaibullin, *Surf. Sci*. **395**, L242 (1998).
4. M. Quinten, A. Heilmann, and A. Kiesow, *Appl. Phys. B* **68**, 707 (1999).

5. P. T. Townsend, P. J. Chandler, and L. Zhang, *Optical Effects of Ion Implantation*, Cambridge University Press, Cambridge (1994).
6. J. Davenas, A. Perez, P. Thevenard, and C. H. S. Dupuy, *Phys. Stat. Sol. A* **19**, 679 (1973).
7. G. W. Arnold, *J. Appl. Phys.* **46**, 4466 (1975).
8. N. C. Koon, D. Weber, P. Pehrsson, and A. I. Sindler, *Mater. Res. Soc. Symp. Proc.* **27**, 445 (1984).
9. Y. Wu, T. Zhang, Y. Zhang, H. Zhang, H. Zhang, and G. Zhou, *Nucl. Instr. Meth. B* **173**, 292 (2001).
10. Y. Wu, T. Zhang, H. Zhang, X. Zhang, Z. Deng, and G. Zhou, *Nucl. Instr. Meth. B* **169**, 89 (2000).
11. K. Ogawa, U.S. Patent 4,751,100 (1988).
12. R. I. Khaibullin, V. N. Popok, V. V. Bazarov, E. P. Zheglov, B. Z. Rameev, C. Okay, L. R. Tagirov, and B. Aktas, *Nucl. Instr. Meth. B* **191**, 810 (2002).
13. V. N. Popok, R. I. Khaibullin, V. V. Bazarov, V. F. Valeev, V. Hnatowicz, A. Mackova, and V. B. Odzhaev, *Nucl. Instr. Meth. B* **191**, 695 (2002).
14. V. Yu. Petukhov, V. A. Zhikharev, N. R. Khabibullina, and I. B. Khaibullin, *Vysokochist. Veshchestva* **3**, 45 (1993) [Russian].
15. V. Yu. Petukhov, V. A. Zhikharev, I. F. Makovskii, Yu. N. Osin, M. A. Mitryaikina, I. B. Khaibullin, and S. N. Abdullin, *Poverhnost* **4**, 27 (1995) [Russian].
16. V. Petukhov, V. Zhikharev, M. Ibragimova, E. Zheglov, V. Bazarov, and I. Khaibullin, *Solid State Commun*. **97**, 361 (1996).
17. V. Yu. Petukhov, M. I. Ibragimova, N. P. Khabibullina, S. V. Shulyndin, Yu. N. Osin, E. P. Zheglov, T. A. Vakhonina, and I. B. Khaibullin, *Polym. Sci. A* **43**, 1154 (2001). Translated from *Vysokomol. Soedin. A* **43**, 1973 (2001) [Russian].
18. V. V. Bazarov, V. Yu. Petukhov, V. A. Zhikharev, and I. B. Khaibullin, *Mater. Res. Soc. Symp. Proc*. **388**, 417 (1995).
19. R. I. Khaibullin, Yu. N. Osin, A. L. Stepanov, and I. B. Khaibullin, *Vacuum* **51**, 289 (1998).
20. R. I. Khaibullin, Yu. N. Osin, A. L. Stepanov, and I. B. Khaibullin, *Nucl. Instr. Meth. B* **148**, 1023 (1999).
21. R. I. Khaibullin, V. A. Zhikharev, Yu. N. Osin, E. P. Zheglov, I. B. Khaibullin, B. Z. Rameev, and B. Aktas, *Nucl. Instr. Meth. B* **166–167**, 897 (2000).
22. B. Z. Rameev, B. Aktas, R. I. Khaibullin, V. A. Zhikharev, Yu. N. Osin, and I. B. Khaibullin, *Vacuum* **58**, 551 (2000).
23. A. L. Stepanov, R. I. Khaibullin, S. N. Abdullin, Yu. N. Osin, and I. B. Khaibullin, *Mater. Res. Soc. Symp. Proc.* **343**, 161 (1994).
24. A. L. Stepanov, R. I. Khaibullin, S. N. Abdullin, Yu. N. Osin, V. F. Valeev, and I. B. Khaibullin, *Pros. Inst. Phys. Conf. Ser*. **147**, 357 (1995).
25. S. N. Abdullin, A. L. Stepanov, R. I. Khaibullin, F. V. Valeev, Yu. N. Osin, and I. B. Khaibullin, *Phys. Solid State* **38**, 1412 (1996) Translated from *Fiz. Tverdogo Tela* **38**, 2574 (1996) [Russian].

26. S. N. Abdullin, A. L. Stepanov, R. I. Khaibullin, and I. B. Khaibullin, Russian Federation Patent 2096835 (1996).
27. S. N. Abdullin, A. L. Stepanov, Yu. N. Osin, R. I. Khaibullin, and I. B. Khaibullin, *Surf. Coat. Techn.* **106**, 214 (1998).
28. R. I. Khaibullin, C. N. Abdullin, A. L. Stepanov, Yu. N. Osin, and I. B. Khaibullin, *Tech. Phys. Lett*. **22**, 112 (1996). Translated from *Pisma Zh. Techni. Fiz.* **22**, 48 (1996) [Russian].
29. I. B. Khaibullin, R. I. Khaibullin, S. N. Abdullin, A. L. Stepanov, Yu. N. Osin, V. V. Bazarov, and S. P. Kurzin, *Nucl. Instr. Methods B* **127–128**, 685 (1997).
30. K. Yoshida and M. Iwaki, *Nucl. Instr. Methods B* **19–20**, 878 (1987).
31. T. Kobayashi, T. Iwata, Y. Doi, and M. Iwaki, *Nucl. Instr. Methods B* **175–177**, 548 (2001).
32. Y. Wu, T. Zhang, Y. Zhang, G. Zhou, H. Zhang, and X. Zhang, *Surf. Coat. Techol*. **148**, 221 (2001).
33. A. L. Stepanov, S. N. Abdullin, R. I. Khaibullin, Yu. N. Osin, and I. B. Khaibullin, *Proc. R. Micr. Soc.* **29**, 226 (1994).
34. A. L. Stepanov, S. N. Abdullin, V. Yu. Petukhov, Yu. N. Osin, R. I. Khaibullin, and I. B. Khaibullin, *Philos. Mag. B* **80**, 23 (2000).
35. A. L. Stepanov, V. N. Popok, I. B. Khaibullin, and U. Kreibig, *Nucl. Instr. Meth. B* **191**, 473 (2002).
36. Y. Wu, T. Zhang, A. Liu, and G. Zhou, *Surf. Coat. Techol*. **157**, 262 (2002).
37. A. L. Stepanov, R. I. Khaibullin, and I. B. Khaibullin, *Philos. Mag. Lett*. **77**, 261 (1998).
38. A. L. Stepanov, S. N. Abdullin, R. I. Khaibullin, V. F. Valeev, Yu. N. Osin, V. V. Bazarov, and I. B. Khaibullin, *Mater. Res. Soc. Symp. Proc.* **392**, 267 (1995).
39. A. L. Stepanov, S. N. Abdullin, R. I. Khaibullin, and I. B. Khaibullin, Russian Federation Patent 97 109708 (010137) (1997).
40. G. R. Rao, K. Monar, E. H. Lee, and J. R. Treglio, *Surf. Coat. Technol*. **64**, 69 (1994).
41. G. Mie, *Ann. Phys.* (*Leipzig*) **25**, 377 (1908).
42. M. A. Khashan and A. Y. Nassif, *Opt. Commun.* **188**, 129 (2001).
43. D. V. Sviridov, *Russian Chem. Rev.* **71**, 315 (2002).
44. A. L. Stepanov and D. E. Hole, *Recent Res. Dev. Appl. Phys.* **5**, 1 (2002).
45. V. B. Odzhaev, I. P. Kozlov, V. N. Popok, and D. V. Sviridov, *Ion Implantation into Polymers*, Belarusk. Gos. University, Minsk (1998) [Russian].
46. S. Deying, Y. Saito, and S. Suganomata, *Jpn. J. Appl. Phys.* **33**, L966 (1994).
47. W. Scheunemann and H. Jäger, *Z. Phys.* **265**, 441 (1973).
48. M. Quinten, *Z. Phys. B* **101**, 211 (1996).
49. U. Kreibig, *J. Phys. F 4*, **999** (1974).
50. P. B. Johnson and R. W. Christy, *Phys. Rev. B* **6**, 4370 (1972).
51. B. Pignataro, M. E. Fragala, and O. Puglisi, *Nucl. Instr. Methods B* **131**, 141 (1997).

52. E. D. Palik, *Handbook of Optical Constants of Solids*, Academic, London (1997).
53. A. Aden and M. Kerker, *J. Appl. Phys.* **22**, 1242 (1951).
54. J. Sinzig and M. Quinten, *Z. Phys. D* **26**, 242 (1993).
55. H. Wang, S. P. Wong, W. Y. Cheung, N. Ke, M. F. Chiah, H. Liu, and X. X. Zhang, *J. Appl. Phys.* **88**, 2063 (2000).
56. V. I. Ivanov-Omskii, A. V. Tolmatchev, and S. G. Yastrebov, *Philos. Mag. B* **73**, 715 (1996).
57. H. Biederman, Z. Chmel, A. Fejfar, M. Misina, and J. Pesicka, *Vacuum* **40**, 377 (1990).
58. O. Stenzel, H. Kupfer, T. Pfeifer, A. Lebedev, and S. Schulze, *Opt. Mater.* **15**, 159 (2000).
59. U. Kreibig, *Handbook of Optical Properties*, Vol. 2: *Optics of Small Particles, Interfaces, and Surfaces*, edited by R. E. Hummel and P. Wissmann, CRC, London (1997).
60. J. Hölzl, F. Schulte, and H. Wagner, *Solid Surface Physics*, Springer, Berlin (1979).
61. U. Kreibig, M. Gartz, and A. Hilger, *Ber. Bunssenges. Phys. Chem.* **101**, 1593 (1997).